

Spontaneous surface plasmon polariton decay of band-edge excitons in quantum dots near a metal surface

Qiang Gao ^{1,2,3}, Zhi Lin ¹, Xiaoguang Li ^{1,*} and Zhenyu Zhang²

¹*Institute for Advanced Study, Shenzhen University, Shenzhen, 518060, China*

²*International Center for Quantum Design of Functional Materials (ICQD), Hefei National Laboratory for Physical Sciences at the Microscale, and Synergetic Innovation Center of Quantum Information and Quantum Physics,*

University of Science and Technology of China, Hefei, Anhui 230026, China

³*Department of Physics, University of Texas at Austin, Austin, Texas 78712, USA*



(Received 25 September 2020; revised 4 January 2021; accepted 7 January 2021; published 15 January 2021)

Surface plasmon polaritons (SPPs) due to their subwavelength nature could significantly modify electronic transition behaviors in various optoelectronic systems. Here, using a model system with a spherical quantum dot (QD) close to a flat metal surface, we show that the conventional forbidden optical transitions in a QD could be largely enabled by the spontaneous SPP decay. The electronic states of the QD are approximated by a Bloch state combined with wave functions in a spherical potential well, which provides multiple hole states with mixed electronic multipoles. Moreover, the SPP is quantized by using a canonical quantization scheme followed by a Green's function approach to introduce its dissipation. In particular, we find that when the SPP dissipation is included, the spontaneous decay of the corresponding QD exciton is dominated by the transition into the off-resonance mode of SPPs with large momenta. Also, we have studied the dependence of spontaneous decay rates on the size and crystal orientation of a QD, the distance between the QD and metal surface, and the linewidth of SPPs. Some useful scaling relations have been revealed, and the multipole transitions are found to be comparable with the dipole transition under specific system parameters. These findings have important implications for our understanding of the electronic transition at a metal near field and might prove instrumental for the future design of plasmonic and QD devices.

DOI: [10.1103/PhysRevB.103.035416](https://doi.org/10.1103/PhysRevB.103.035416)

I. INTRODUCTION

Surface plasmon describes the collective motion of the conduction electrons near a metal surface. It can strongly couple with an electromagnetic field to form the hybrid mode known as surface plasmon polaritons (SPPs) [1]. The SPP inherits a large momentum of electronic collective motion, possessing a much shorter wavelength than light, confined at the metal near field. Many intriguing applications, including plasmonic lithography [2], subwavelength optics [1,3], and surface-enhanced Raman spectroscopy [4,5], are rooted in the short wavelength and/or near-field enhancement of such excitations [6,7]. Due to its short-wavelength nature, forbidden transitions under the conventional electric dipole selection rule of optic transitions are enabled by decaying into SPPs. The near-field enhancement of the SPP, meanwhile, provides a vast optical local density of state (LDOS) and thus enlarges the transition rates of different channels by Purcell effect, making it essential for electronic transitions. In the past decade, considerable efforts have been devoted to exploring the effects of this shrinking light [7–11].

Quantum dots (QDs) provide an attractive platform for tailoring light-matter interaction, especially when combined with the shrinking light of metal nanostructures. The physics and in particular the optical properties of QDs can be effectively and precisely controlled by changing the shape, size,

and chemical composition of the nanoparticles [12], giving rise to a rich variety of applications, such as light-emitting diodes (LEDs) [13,14], solar cells [15], and quantum information devices [16]. In particular, due to the mesoscopic size and large oscillator strength of QDs, they can fully utilize the short wavelength and strong LDOS enhancement of electromagnetic fields, rendering the QD or QD-metal hybrid systems many intriguing phenomena. For example, due to the breakdown of the dipole approximation, the decay of a QD exciton could depend on the orientation [17]. The oscillator strength of QDs can be tuned by changing the particle size [18,19] or applying a magnetic field [20] to control the wave function of their excitons. Also, multipole transitions in asymmetry QDs have been observed experimentally [21]. On the theoretical side, we note that most of the previous studies on the hybrid systems focused on a simply QD electronic structure, i.e., a phenomenological dipole or quadrupole transition [22], or their interference [23]. It will be very interesting to get into detailed electronic states of QDs, by considering more realistic and complex transition channels of QDs under diverse control parameters. Such a systematic study is expected to improve the understanding of fundamental properties of QD-metal hybrid systems, which is essential to realize the full potential of the systems.

In this study, we investigate a prototypical hybrid system composed of a spherical QD proximity to a metal surface, by using a full quantum mechanical approach with the detailed electronic states of a QD and a dissipative SPP at a metal

*Corresponding author: xgli@szu.edu.cn

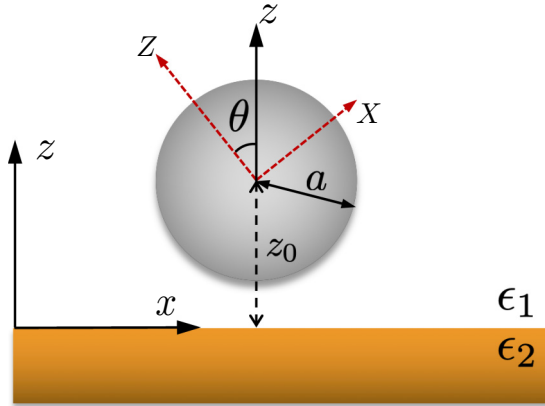


FIG. 1. The sketch of the system with a spherical QD above a metal surface in vacuum. We consider two different coordinates: one is the coordinate xyz fixed by the metal surface, and the other is the coordinate XYZ depicted by the red dashed lines attach to the crystal symmetry axes.

surface. The electronic states of the QD are approximated by a Bloch state combined with wave functions in a spherical potential well. The SPP is quantized by using a canonical quantization scheme followed by a Green's function approach to introduce its dissipation. In analogy to a spherical CdTe QD, we obtain different hole states categorized by the parity and angular momentum. Due to an effective spin-orbit coupling, the hole states involve the envelope functions with different angular momenta, and thus gain mixed electronic multipoles. The spontaneous decay rate of the exciton is then obtained by using the Fermi's golden rule. In particular, we find that the introduction of the SPP dissipation allows the exciton decay into off-resonance modes of the SPP. This "nonradiative" SPP decay strongly enhances the total spontaneous decay rate, comparing with the "radiative" decay when only consider a nondissipative SPP. In addition, we evaluate the spontaneous decay for different excitonic states, which includes the different multipole transitions and their interference. The results indicate that the multipole transition can have a non-negligible contribution for the spontaneous decay under specific system parameters. The dependence of the decay rates on the size and crystal orientation of a QD, the distance between the QD and metal surface, and the linewidth of SPPs, are also evaluated. This study may prove instrumental in the design of future high-efficiency energy devices, such as QD LEDs and QD solar cells. Understanding these excitonic optical properties is much required in order to optimally engineer QDs for controllable light-matter interactions.

This paper is organized as follows. In Sec. II we present theoretical models, including the quantization of a dissipative SPP, the electronic states in QDs, and the spontaneous SPP decay rate. In Sec. III, we compare in detail the deexcitation processes of the excitons mediated by free photons and the SPPs. We close the paper with a summary in Sec. IV.

II. THEORETICAL MODELS

The system of interest, sketched in Fig. 1, is a QD of radius a close to an adjacent metal surface, with the distance

z_0 between the QD center and metal surface. The angle between the Z axis of the QD crystal and the z axis normal to the metal surface is θ . The metal surface supports SPPs of momenta k far greater than that of free photons. Therefore, the conventional dipole approximation (long-wavelength approximation) cannot be applied, and the multipole components of the SPPs will largely modify the transition behaviors of the QD excitons. In addition, due to the dissipation of the SPP, the dispersion curve of the SPP gets a finite broadening Γ . For the energy transition from a QD exciton to an SPP at an energy ω , we need to integrate over k . Consequently, for the multipole transition proportional to the high-order k terms, a significant contribution from high- k region can be expected.

In this section, we first describe the quantization method of a dissipative SPP, then evaluate electronic states in a QD, and finally give the spontaneous SPP decay rate of the QD excitonic state. We will see how the above parameters, including the radius a , distance z_0 , angle θ , energy ω , broadening Γ , and momentum k , affect the decay rate.

A. Quantization of dissipative SPPs

For the sake of completeness and self-containing presentation, we first write the canonical quantization result of a nondissipative SPP [24]. Then, different from the widely used macroscopic QED scheme [7,25], we introduce the dissipation using a Green's function approach by considering a bosonic pool surrounding the nondissipative SPPs [26]. Both methods eventually bring a finite broadening to the SPP mode described approximately by the dispersion curve of the nondissipative SPPs. The advantage of the method used here is that it can straightforwardly introduce the energy shifting and broadening of the SPP by a phenomenological way with clear underlying physics, while it keeps the essential differences between the SPP and free photon field, i.e., the different dimensionality, field polarization, and energy dispersion. Consequently, clear insight can be revealed.

In analogy to the quantized photon field, we can write the quantized vector potential operator of an SPP as [24]

$$\hat{\mathbf{A}}(\mathbf{r}, t) = \sum_{\mathbf{k}} \sqrt{\frac{\hbar}{2\epsilon_0\omega_{\mathbf{k}}SL(\omega_{\mathbf{k}})}} \left(\mathbf{e}_{\mathbf{k}} - \frac{k}{q_j} \mathbf{e}_z \right) \times (\hat{a}_{\mathbf{k}} e^{-i\omega_{\mathbf{k}}t} + \hat{a}_{-\mathbf{k}}^\dagger e^{i\omega_{\mathbf{k}}t}) e^{i\mathbf{k}\cdot\boldsymbol{\rho}} e^{iq_j z}, \quad (1)$$

where $\mathbf{r} = (\boldsymbol{\rho}, z)$ is divided in the coordinates $\boldsymbol{\rho}$ parallel and z perpendicular to the metal-dielectric interface; S and \mathbf{k} are, respectively, the quantized area and wave vector parallel to the interface; $L(\omega)$ and q are, respectively, the effective mode length and wave number perpendicular to the interface; $(\mathbf{e}_{\mathbf{k}} - \frac{k}{q_j} \mathbf{e}_z)$ indicates the polarization of the field; $\hat{a}_{\mathbf{k}}$ ($\hat{a}_{\mathbf{k}}^\dagger$) is the annihilation (creation) operator, labeled with the wave vector \mathbf{k} ; $\omega_{\mathbf{k}}$ depending on k is the frequency of the field. The wave number q is a complex number, defined as

$$q^2 = \begin{cases} q_1^2 = \epsilon_1(\omega)\omega^2/c^2 - k^2 & \text{for } z > 0, \\ q_2^2 = \epsilon_2(\omega)\omega^2/c^2 - k^2 & \text{for } z < 0, \end{cases} \quad (2)$$

which is a complex number and guarantees the field decaying away from interface in both air and metal regions with dielectric functions ϵ_1 and ϵ_2 , respectively.

The dispersion relation between wave vector k and ω can be obtained by solving Maxwell's equations as

$$k^2 = \left(\frac{\omega}{c}\right)^2 \frac{\epsilon_1 \epsilon_2}{\epsilon_1 + \epsilon_2}. \quad (3)$$

By considering a dielectric setup with $\epsilon_1 = 1$ and

$$\epsilon_2(\omega) = 1 - \frac{\omega_p^2}{\omega^2}, \quad (4)$$

describing the dielectric function of a nondissipative material with plasmon frequency ω_p , we can explicitly write the dispersion relation of the SPP as

$$\omega_k = \left(\frac{\omega_p^2}{2} + k^2 c^2 - \sqrt{\frac{\omega_p^4}{4} + k^4 c^4}\right)^{1/2}, \quad (5)$$

where c is the speed of light. This dispersion will be changed as the dissipation is introduced. A detailed discussion about this change and its relation with the quantization results given below are shown in Appendix A.

The effective mode length $L(k)$ is evaluated to ensure the each SPP mode with wave vector k having the energy $\hbar\omega_k$. Based on the above dielectric function, it can be obtained by following the procedure in Ref. [24] as

$$L(k) = \frac{-1}{2|q_1|} \left(1 - \frac{1}{\epsilon_2}\right) \left(\frac{1}{\epsilon_2} + \epsilon_2\right). \quad (6)$$

Physically, $L(k)$ describes the SPP field decay length normal to the metal surface. Because the field decay lengths in air and metal regions are different, and depend on the corresponding dielectric functions, the form of this normalization factor looks complicated. However, if one considers the large- k limit, which implies $\omega_k = \omega_p/\sqrt{2}$ and $\epsilon_2 = -1$ from Eqs. (4) and (5), the effective mode length is simply the direct sum of the decay lengths in air and metal as $L = \frac{2}{|q_1|} \simeq \frac{1}{|q_1|} + \frac{1}{|q_2|}$.

By now, we see that the main differences between the quantization of the SPP field and the free photon field are the volume regulator V , the field polarization, and the dispersion ω_k . Now, we introduce the damping mechanism by connecting the SPP with an environment that is characterized by a bosonic pool [27,28]. The total Hamiltonian reads as [26]

$$H = \sum_k \left[\hbar\omega_k \hat{a}_k^\dagger \hat{a}_k + \int_0^\infty d\omega \hbar\omega \hat{C}_{k,\omega}^\dagger \hat{C}_{k,\omega} + \hbar \int_0^\infty d\omega V(\omega, \mathbf{k}) (\hat{a}_k + \hat{a}_{-k}^\dagger) (\hat{C}_{k,\omega} + \hat{C}_{-k,\omega}^\dagger) \right], \quad (7)$$

where $\hat{C}_{k,\omega}$ ($\hat{C}_{k,\omega}^\dagger$) is the the annihilation (creation) operator of a single boson with the momentum \mathbf{k} and energy ω , and $V(\omega, \mathbf{k})$ is the coupling strength between the boson and SPP.

To obtain the new quantized vector potential $\hat{A}(\mathbf{r}, t)$ including the dissipation, one could first diagonalize the Hamiltonian in Eq. (7). The diagonalization can be performed exactly using the method given by Huttner and Barnett [29], which allows us to write the Hamiltonian in the following form:

$$H = \sum_k \int_0^\infty d\omega \hbar\omega \hat{f}_{k,\omega}^\dagger \hat{f}_{k,\omega}, \quad (8)$$

where the new operator $\hat{f}_{k,\omega}$ ($\hat{f}_{k,\omega}^\dagger$), so-called dressed SPP (dSPP), describes the annihilation (creation) of a SPP in the damping environment. Here, the integration of ω implies that for a certain wave number \mathbf{k} , the energy of the dSPP exhibits a broadening due to the bosonic pool. Then, using the $\hat{f}_{k,\omega}$ ($\hat{f}_{k,\omega}^\dagger$), we can rewrite the quantized vector potential $\hat{A}(\mathbf{r}, t)$ in Eq. (1) as

$$\begin{aligned} \hat{A}(\mathbf{r}, t) = & \sum_k \sqrt{\frac{\hbar}{2\epsilon_0\omega_k SL(\omega_k)}} \left(\mathbf{e}_k - \frac{k}{q_j} \mathbf{e}_z\right) e^{i\mathbf{k}\cdot\mathbf{r}} e^{iq_j z} \\ & \times \int_0^\infty d\omega [N(\omega, \mathbf{k}) \hat{f}_{k,\omega} e^{-i\omega t} \\ & + N^*(\omega, -\mathbf{k}) \hat{f}_{-\mathbf{k},\omega}^\dagger e^{i\omega t}], \end{aligned} \quad (9)$$

where the normalization factor $N(\omega, \mathbf{k})$ should satisfy

$$\int_0^\infty d\omega |N(\omega, \mathbf{k})|^2 = 1. \quad (10)$$

In this study, to obtain the square modulus of the above factor, we adopt a Green's function method [26]. According to the discussion in Appendix B, the normalization factor can be obtained from the relation

$$|N(\omega, \mathbf{k})|^2 = -\frac{1}{\pi} \text{Im}[G(\omega, \mathbf{k})], \quad (11)$$

where $G(\omega, \mathbf{k})$ is the Green's function of the dSPP described by the Hamiltonian in Eq. (7).

The lowest-order Feynman diagram of a propagating SPP connected with the bosonic pool can be drawn as

$$\text{---} \overset{spp}{\sim} \bullet \text{---} \overset{b}{\sim} \bullet \text{---} \overset{spp}{\sim} \text{---}, \quad (12)$$

where the wavy line denotes the propagator of the nondissipative SPP, the dashed line denotes the propagator of a boson in the bosonic pool. Following Dyson's method, we obtain the dSPP denoted by a coiled line as

$$\text{---} \overset{dspp}{\sim} \text{---} = \text{---} \overset{spp}{\sim} \text{---} + \text{---} \overset{spp}{\sim} \bullet \text{---} \overset{b}{\sim} \bullet \text{---} \overset{dspp}{\sim} \text{---}. \quad (13)$$

This diagram can be translated into the Green's function as

$$G = G_0 + G_0 V G_b V G. \quad (14)$$

Then, the G , denoting the Green's function of the dSPP, can be solved as

$$G = \frac{G_0}{1 - G_0 V G_b V}, \quad (15)$$

where G_0 , denoting the Green's function of the nondissipative SPP, is written as

$$G_0 = \frac{1}{\omega - \omega_k + i\eta} \quad (16)$$

with an infinitesimal constant η (see Appendix B for details); G_b describes the propagator of a boson from the bosonic pool. The G_b has the similar form as the nondissipative SPP in Eq. (16), and can be written by absorbing the coupling strength V as

$$G_b V^2 = \int_0^\infty \frac{|V(\omega', \mathbf{k})|^2}{\omega - \omega' + i\eta} d\omega'. \quad (17)$$

Finally, the Green's function G can be explicitly written as

$$G = \frac{1}{\omega - \omega_k - (\delta\omega_k + i\Gamma/2)} \quad (18)$$

with

$$\delta\omega_k - i\Gamma/2 = G_b V^2 = \int_0^\infty \frac{|V(\omega', \mathbf{k})|^2}{\omega - \omega' + i\eta} d\omega', \quad (19)$$

where $\delta\omega_k$ and Γ indicate, respectively, the energy shifting and linewidth broadening due to the bosonic pool.

By inserting the result of G in Eq. (11) and by making a further transition

$$\frac{(2\pi)^2}{S} \sum_{\mathbf{k}} \rightarrow \int d\mathbf{k}, \quad (20)$$

and a substitution $\beta = |q_1| = \sqrt{k^2 - \epsilon_1 \omega^2 / c^2}$, we can write the vector potential of the dSPP as

$$\hat{\mathbf{A}}(\mathbf{r}, t) = \int_0^\infty d\omega \int d\mathbf{k} \left(\mathbf{e}_k + i \frac{k}{\beta} \mathbf{e}_z \right) e^{i\mathbf{k} \cdot \boldsymbol{\rho}} e^{-\beta z} \times [A(\omega, \mathbf{k}) \hat{f}_{\mathbf{k}, \omega} e^{-i\omega t} + A^*(\omega, -\mathbf{k}) \hat{f}_{-\mathbf{k}, \omega}^\dagger e^{i\omega t}] \quad (21)$$

with amplitude $A(\omega, \mathbf{k})$ defined as

$$|A(\omega, \mathbf{k})|^2 = \frac{\hbar}{8\pi^2 \epsilon_0 \omega_k L(\omega_k)} \frac{\Gamma/2\pi}{(\omega - \omega_k - \delta\omega_k)^2 + \frac{\Gamma^2}{4}}. \quad (22)$$

Here, the Lorentz function in the amplitude clearly signals a dissipative SPP resonance with the energy $\omega = \omega_k + \delta\omega_k$ and broadening Γ .

In order to elucidate the connection between the SPP dissipation and the decay of the QD exciton, we show a numerical result for the amplitude $|A(\omega, \mathbf{k})|^2$ of the dSPP in Fig. 2(a), where we approximate the energy shifting $\delta\omega_k = 0$ and linewidth broadening $\Gamma = 0.05 \omega_p$. The validation of this approximation has been carefully discussed in Appendix A. The solid curves in Fig. 2(b) display the broadening of $|A(\omega, \mathbf{k})|^2$ in respect to k for a fixed ω . Due to the energy broadening, the amplitude of the dSPP exhibits a finite value in the high- k region. Close to the surface plasmon resonant frequency ω_{sp} , the value at large k becomes comparable with the resonant peak, because the SPP becomes nondispersive. Later, when we consider the decay rate of QD excitons, we need to integrate over the momentum k for a fixed exciton energy ω [30]. Consequently, a large contribution can be expected from the ‘‘off-resonance’’ high- k region, especially for the multipole transitions involving high-order k terms. Since these off-resonance modes represent the mixing states between the SPP and the bosonic pool, in this study, we call the transition from a QD exciton to these modes as a nonradiative SPP decay, while the transition into the resonant mode as a radiative SPP decay.

We note that we have ignored the nonclassical correction for the SPP dispersion and LDOS [31], namely, we did not consider the redshift and probably larger broadening of the SPP resonance at a large k . In addition, we are not trying to discuss any real materials, for which the plasmon dispersion should be calculated more carefully, or consider other effects, such as the nonlocal correction. However, within an ideal Drude model, we show that as dissipation is introduced to

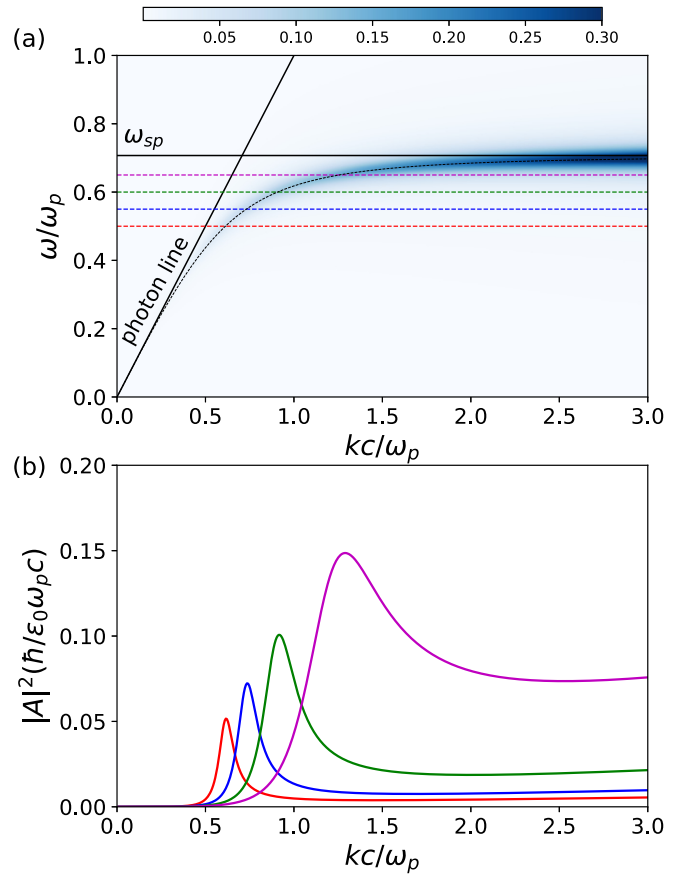


FIG. 2. The value of $|A(\omega, \mathbf{k})|^2$ is mapped as the energy ω and momentum k in (a), where the dashed lines indicate $|A(\omega, \mathbf{k})|^2$ at $\omega/\omega_p = 0.5, 0.55, 0.6,$ and 0.65 corresponding to the solid curves with the same color in (b).

the SPP, it allows the nonradiative decay due to the induced off-resonance distribution, and then the corresponding distribution in the high- k region can largely modify the multipole transition rate of a nearby emitter.

B. Electronic states of excitons in QDs

To investigate a system with more realistic band structures, including different types of transitions, we consider a spherical CdTe QD, which has an s -orbital conduction band and a p -orbital valence band. More specifically, we consider the cubic crystal lattice for simplicity. We believe the concept demonstrated in this simple setup could be applied to other QDs with different materials and crystal structures. One example is that the validation of using cubic zinc-blende lattice to approximate wurtzite lattice has been shown in Ref. [32]. In CdTe, and many other II-VI and III-V compounds, due to the spin-orbit coupling induced valence band splitting, the direct interband transition is between the conduction band Γ_{6c} and valence band Γ_{8v} .

For this spherical QD, we evaluate the electronic state by using the envelope-function method [12,32,33]. Within this method, the electronic wave function consists of two parts written as

$$\Phi(\mathbf{r}) = \psi_{l,m}(\mathbf{r}) u_{n,k=0} = R_l(r) Y_l^m(\Omega) u_{n,k=0}, \quad (23)$$

where $\psi_{l,m}(\mathbf{r})$ describes the wave function in an infinite spherical potential well, including the radial part $R_l(r)$ and the spherical harmonic function $Y_l^m(\Omega)$ with angular momentum quantum number l and magnetic quantum number m ; u_n describing the motion in a primitive cell, represents the Bloch function of the corresponding bulk band at the Γ point with quantum number n labeling the different bands.

The lowest electronic state in the conduction band Γ_{6c} is mainly contributed by s -orbital electron, we write the corresponding Bloch state as $|S\alpha\rangle$ with S standing for its S symmetry and $\alpha = \uparrow, \downarrow$ standing for the electron spin projection. Combining this Bloch state and the ground state of the infinite spherical potential well with angular momentum $l = 0$, one obtains the wave function of the electron state as

$$\begin{aligned}\Phi_\alpha^e(\mathbf{r}) &= f(r)Y_0^0(\Omega)|S\alpha\rangle \\ &= \sqrt{\frac{2}{a}} \frac{\sin(\pi r/a)}{r} Y_0^0(\Omega)|S\alpha\rangle,\end{aligned}\quad (24)$$

where a is the radius of the QD and $f(r)$ gives the radial part of the envelope function.

For the hole states in the valence band, the wave functions become much more complicated due to the heavy- and light-hole bands are degenerate at the Γ point of the bulk band. In bulk, these two bands are labeled by the total angular momentum $J = \frac{3}{2}$ due to the spin-orbit coupling between the p orbit and spin- $\frac{1}{2}$ electron. In a spherical QD, these heavy- and light-hole states will be mixed, and the eigenstates should be labeled by a total angular momentum F due to the ‘‘spin-orbit coupling’’ between the orbital angular momentum l in the spherical quantum well and the ‘‘spin’’ $J = \frac{3}{2}$ bulk electron. This problem is first studied by Luttinger [34], and then simplified by Baldereschi and Lipari using the so-called ‘‘spherical approximation’’ [35,36]. The details to obtain the radial part of the envelope function can be found in Appendix C.

The Bloch function of the hole state can be described as the state $|J\mu\rangle$ with angular momentum $J = \frac{3}{2}$ and the corresponding magnetic quantum number $\mu = \pm\frac{3}{2}$ and $\pm\frac{1}{2}$ for heavy- and light-hole states, respectively. The total angular momentum is described by $|FM\rangle$, where $\vec{F} = \vec{J} + \vec{l}$ is the total angular momentum and $M = \mu + m$ is the corresponding magnetic quantum number. The ground state of the hole state is found to have $F = \frac{3}{2}$ [32]. So, the angular momentum l satisfying $|F - J| \leq l \leq F + J$ is in the range of $0 \leq l \leq 3$. Moreover, because the total Hamiltonian commutes with parity, the states with $F = \frac{3}{2}$ can be further categorized by parties, corresponding to the states composed by $l = 0, 2$ and $l = 1, 3$, respectively. Figure 3 shows a schematic plot of the electronic states in QDs. For convenience, we call the states with $M = \pm\frac{3}{2}$ and $\pm\frac{1}{2}$ as high-spin (HS) and low-spin (LS) hole states, respectively. The final results of the hole states are written as

$$\Phi_M^{h,o} = 2 \sum_{l=0,2} R_l(r) \sum_{m+\mu=M} \begin{bmatrix} \frac{3}{2} & l & \frac{3}{2} \\ \mu & m & -M \end{bmatrix} Y_l^m(\Omega) u_\mu \quad (25)$$

for the *odd* state and

$$\Phi_M^{h,e} = 2 \sum_{l=1,3} R_l(r) \sum_{m+\mu=M} \begin{bmatrix} \frac{3}{2} & l & \frac{3}{2} \\ \mu & m & -M \end{bmatrix} Y_l^m(\Omega) u_\mu \quad (26)$$

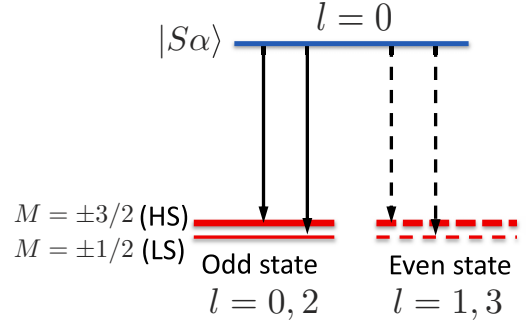


FIG. 3. The schematic plot of the electronic states in the spherical QD. The blue solid line indicates the electron state. The red thick (thin) line indicates the $M = \pm\frac{3}{2}$ ($\pm\frac{1}{2}$) hole states, and the solid (dashed) line indicates the odd (even) state. The black solid (dashed) arrows represent the dipole allowed (forbidden) transitions.

for the *even* state, where the radial function $R_l(r)$ can be found in Appendix C, the big square brackets denote the Wigner $3j$ symbol, and u_μ are the fourfold Bloch functions of the valence band Γ_{8v} , written as [32]

$$\begin{aligned}u_{3/2} &= \frac{1}{\sqrt{2}}(X + iY) \uparrow, \\ u_{-3/2} &= \frac{i}{\sqrt{2}}(X - iY) \downarrow, \\ u_{1/2} &= \frac{1}{\sqrt{6}}[(X + iY) \downarrow - 2Z \uparrow], \\ u_{-1/2} &= \frac{i}{\sqrt{6}}[-(X - iY) \uparrow + 2Z \downarrow].\end{aligned}\quad (27)$$

The states X , Y , and Z denote the three orthogonal p -orbit states of the valence band.

C. Spontaneous SPP decay of the excitons

Now, we have quantum states of both the SPP and QD exciton ready for the further evaluation. To evaluate the spontaneous decay rate, we assume that the initial state $|i\rangle = |\Phi, 0\rangle$ and final state $|f\rangle = |\Phi, 1_{\mathbf{k}}\rangle$, where 0 in the initial state indicates the SPP vacuum, while $1_{\mathbf{k}}$ indicates one SPP with the wave number \mathbf{k} . Therefore, by considering the time average, the decay rate can be given by Fermi’s golden rule as

$$\Gamma_{M,\alpha} = \frac{2\pi}{\hbar^2} \iint d\mathbf{k} d\omega |\langle f | H_{\text{int}} | i \rangle|^2 \delta(\omega - \omega_{eh}), \quad (28)$$

where $H_{\text{int}} = \frac{e}{m} \hat{\mathbf{p}} \cdot \hat{\mathbf{A}}(\mathbf{k})$ is the interacting part of the total Hamiltonian and ω_{eh} is the exciton energy. By integrating over ω and considering the action of the field operator, we obtain

$$\Gamma_{M,\alpha} = \frac{2\pi}{\hbar^2} \frac{e^2}{m^2} \int d\mathbf{k} e^{-2\beta z_0} |A(\omega_{eh}, \mathbf{k})|^2 T_{M,\alpha}(\mathbf{k}) \quad (29)$$

with the term

$$T_{M,\alpha}(\mathbf{k}) = |\langle \Phi_e^e | e^{-\beta z_0 + ikx} \mathbf{e}_p \cdot \hat{\mathbf{p}} | \Phi_M^h \rangle|^2, \quad (30)$$

where $\mathbf{e}_p = \mathbf{e}_x + i\frac{k}{\beta} \mathbf{e}_z$ is the polarization of the SPP field and the coordinate (x, y, z) is measured from the QD center.

The integrand part $T_{M,\alpha}(\mathbf{k})$ includes the important information about the selection rule discussed in this study. To deal with it, we first consider the electrostatic limit with $k \gg \frac{\omega}{c}$ to apply the approximation $\beta \simeq k$ and then expand the exponential factor to the polynomial of r as

$$e^{-kz+ikx} \simeq \sum_{l=0,1,2,3} r^l \mathcal{Y}_l(k, \Omega), \quad (31)$$

where

$$\mathcal{Y}_0(k, \Omega) = \sqrt{4\pi} Y_0^0(\Omega), \quad (32)$$

$$\mathcal{Y}_1(k, \Omega) = k \sqrt{\frac{2\pi}{3}} [-\sqrt{2} Y_1^0 + i(Y_1^{-1} - Y_1^1)], \quad (33)$$

$$\mathcal{Y}_2(k, \Omega) = k^2 \sqrt{\frac{2\pi}{15}} [\sqrt{6} Y_2^0 - 2i(Y_2^{-1} - Y_2^1) - (Y_2^{-2} + Y_2^2)], \quad (34)$$

and

$$\begin{aligned} \mathcal{Y}_3(k, \Omega) = & \frac{k^3}{6} \sqrt{\frac{\pi}{35}} [-2\sqrt{5} Y_3^0 + \sqrt{15} i(Y_3^{-1} - Y_3^1) \\ & + \sqrt{6}(Y_3^{-2} + Y_3^2) - i(Y_3^{-3} - Y_3^3)]. \end{aligned} \quad (35)$$

Here, we note that the unit cell of the QD has a size much smaller than the SPP wavelength. In this case, the oscillation part $e^{-\beta z+ikx}$ can be considered as a constant as it acting on the Bloch functions, and only the envelope function of the electronic state is affected by the variation of this SPP electric field [20,37]. So, the selection rule discussed in this study is explicitly referred to the transition of the envelope function under the SPP field. It is easy to see that when this selection rule applies to the photon, we have the dipole selection rule allowed transition with $\Delta l = 0$.

By separating the Bloch and envelope functions of the electronic state, the term $T_{M,\alpha}(\mathbf{k})$ can be rewritten into the following three different parts as

$$T_{M,\alpha}(\mathbf{k}) = \left| 2 \sum_{l,\mu} \mathcal{I}_{l,\mu}^M(k) K_l C_{\mu\alpha} \right|^2, \quad (36)$$

$$\overline{T_{\pm\frac{1}{2}}^o} = \overline{T_{\pm\frac{1}{2},\uparrow}^o} + \overline{T_{\pm\frac{1}{2},\downarrow}^o} = P^2 J_0^2 \left[1 - \frac{J_2(ka)^2}{J_0} \frac{1}{5} \right] \frac{(7 + 3 \cos^2 \theta)}{12} + P^2 J_2^2 (ka)^4 \frac{(11 - \cos^2 \theta)}{600}, \quad (40)$$

$$\overline{T_{\pm\frac{3}{2}}^o} = \overline{T_{\pm\frac{3}{2},\uparrow}^o} + \overline{T_{\pm\frac{3}{2},\downarrow}^o} = P^2 J_0^2 \left[1 + \frac{J_2(ka)^2}{J_0} \frac{1}{5} \right] \frac{(3 - \cos^2 \theta)}{4} + P^2 J_2^2 (ka)^4 \frac{(31 + 3 \cos^2 \theta)}{600}, \quad (41)$$

$$\overline{T_{\pm\frac{1}{2}}^e} = P^2 J_0^2 \left[\frac{J_1^2(ka)^2 (31 + 3 \cos^2 \theta)}{J_0^2 270} - \frac{J_1 J_3(ka)^4 (1 + \cos^2 \theta)}{J_0^2 105} + \frac{J_3^2(ka)^6 (5 + \cos^2 \theta)}{J_0^2 2940} \right], \quad (42)$$

$$\overline{T_{\pm\frac{3}{2}}^e} = P^2 J_0^2 \left[\frac{J_1^2(ka)^2 (17 - 3 \cos^2 \theta)}{J_0^2 90} + \frac{J_1 J_3(ka)^4 (3 - \cos^2 \theta)}{J_0^2 420} + \frac{J_3^2(ka)^6 (13 + \cos^2 \theta)}{J_0^2 35280} \right], \quad (43)$$

where θ is the angle between the crystal Z axis of the QD and the z axis of the metal surface, and $P = \langle S | \hat{p}_X | X \rangle = \langle S | \hat{p}_Y | Y \rangle = \langle S | \hat{p}_Z | Z \rangle$ is the Kane interband transition matrix

where

$$\mathcal{I}_{l,\mu}^M(k) = \left[\begin{matrix} \frac{3}{2} & l & \frac{3}{2} \\ \mu & m & -M \end{matrix} \right] \int d\Omega Y_0^0 \mathcal{Y}_l(k, \Omega) Y_l^m \quad (37)$$

is the transition amplitude from the angular part of the envelope function, providing the selection rule of the transition

$$K_l = a^l J_l = a^l \int dr r^2 \left(\frac{r}{a} \right)^l f(r) R_l(r) \quad (38)$$

is the transition amplitude from the radius part of the envelope function, giving the size dependence of the transition, and

$$C_{\mu\alpha} = \langle S\alpha | \mathbf{e}_p \cdot \hat{\mathbf{p}} | u_\mu \rangle \quad (39)$$

is the transition amplitude from a unit cell, offering the crystal orientation dependence of the transition.

The term $\mathcal{I}_{0,\mu}^M$ tells us that by considering dipole selection rule $\Delta l = 0$ and the electron state with $l = 0$, only the transition into the odd hole states including the term with $l = 0$ is allowed by the spontaneous photon decay. Therefore, we call the exciton with the odd hole state as a *bright* exciton and that with the even hole state as a *dark* exciton. In the following, we can see that due to the short wavelength of the SPP, the term with $l = 1, 2, 3$ and their interference will have large contributions to the spontaneous SPP decay and, therefore, breaking the conventional dipole selection rule.

The integration of the radius part of the envelope function K_l has been written into the radius-dependent part a^l and a dimensionless term J_l . It is clear that for a QD with a larger size, $l > 0$ term will have a larger contribution. The radius part of the wave function R_l involving the hybridization between the heavy- and light-hole state has been given in Appendix C, where we have evaluated the value of J_l at different ‘‘spin-orbit coupling’’ strengths.

The excitation of the SPP is restricted at the metal surface, which breaks the isotropic property of the spontaneous photon decay in vacuum. Therefore, $C_{\mu\alpha}$ exhibits the crystal orientation dependence as shown in Appendix D. The amplitude of the corresponding transition matrix and an average over the surface plasmon propagating in different azimuthal angle can be done separately. The results can also be found in Appendix D.

After some algebraic manipulations, we obtain the integrand part $T_{M,\alpha}(\mathbf{k})$ for the different excitons as

element [32]. More details of the above equations are given in Appendix E. In addition, we can see that since $J_i > 0$, the transitions due to the interference between different l terms

are always destructive for LS hole and constructive for HS hole states.

III. NUMERICAL RESULTS AND DISCUSSIONS

The results shown in Eqs. (40)–(43) provide abundant physics related to the spontaneous SPP decay. In this section, based on the above analytic results, we provide quantitative results and discussion about the decay rates. Essentially, we compare the decay rates due to free photons and SPPs for systems with different key parameters: the energy of the exciton ω_0 , the linewidth of the SPP Γ , the size a and crystal orientation θ of the QD, and the distance between QD and metal surface z_0 .

First, we evaluate the spontaneous photon decay rate of the bright excitons. Similar to the integrand part $T_{M,\alpha}(\mathbf{k})$ of the SPP transition in Eq. (30), and by considering a different field polarization \mathbf{e}_γ , we evaluate the integrand part of the photon decay as [32]

$$\begin{aligned} T_{1/2,\downarrow}^{\alpha,\gamma}(\theta) &= N_\gamma^2 J_0^2 |\langle S \downarrow | \mathbf{e}_\gamma \cdot \hat{\mathbf{p}} | u_{1/2} \rangle|^2 \\ &= \frac{1}{6} N_\gamma^2 J_0^2 P^2 \sin^2 \theta, \end{aligned} \quad (44)$$

where $N_\gamma = \sqrt{\frac{\hbar}{2\epsilon_0\omega V}}$ is introduced due to the standard photon quantization. Due to the dipole selection rule, the above result only includes the J_0 term. Similarly, for the other bright state transitions, we obtain

$$T_{1/2,\uparrow}^{\alpha,\gamma}(\theta) = \frac{2}{3} N^2 J_0^2 P^2 \cos^2 \theta, \quad (45)$$

$$T_{3/2,\uparrow}^{\alpha,\gamma}(\theta) = \frac{1}{2} N^2 K^2 P^2 \sin^2 \theta, \quad (46)$$

and

$$T_{3/2,\downarrow}^{\alpha,\gamma}(\theta) = 0. \quad (47)$$

Then, by integrating over k , the photon decay rate is obtained as

$$\begin{aligned} \Gamma_{1/2,\downarrow}^{\alpha,\gamma} &= \frac{2\pi}{\hbar^2} \frac{e^2}{m^2} \frac{V}{(2\pi)^3} \sum_{i=1,2} \int d^3\mathbf{k} P_{1/2,\downarrow}^{\alpha,\gamma} \delta(kc - \omega_0) \\ &= \frac{1}{3} \Gamma_0 \end{aligned} \quad (48)$$

with the definition

$$\Gamma_0 = \frac{4}{3} \frac{1}{4\pi\epsilon_0} \frac{\omega_0}{\hbar c^3} \frac{e^2}{m^2} J_0^2 P^2 = \frac{4\alpha}{3} \frac{\omega_0}{m^2 c^2} J_0^2 P^2, \quad (49)$$

where ω_0 represents the transition energy, $\alpha = \frac{e^2}{4\pi\epsilon_0\hbar c}$ is the fine-structure constant, and the summation over i represents the two different polarizations of the photon. Similarly, we find

$$\Gamma_{1/2,\uparrow}^{\alpha,\gamma} = \frac{2}{3} \Gamma_0 \quad (50)$$

and, therefore,

$$\Gamma_{1/2}^{\alpha,\gamma} = \Gamma_{1/2,\uparrow}^{\alpha,\gamma} + \Gamma_{1/2,\downarrow}^{\alpha,\gamma} = \Gamma_0. \quad (51)$$

Actually, we find that all the bright excitons have the same transition rate as

$$\Gamma_{\pm 1/2}^{\alpha,\gamma} = \Gamma_{\pm 3/2}^{\alpha,\gamma} = \Gamma_0. \quad (52)$$

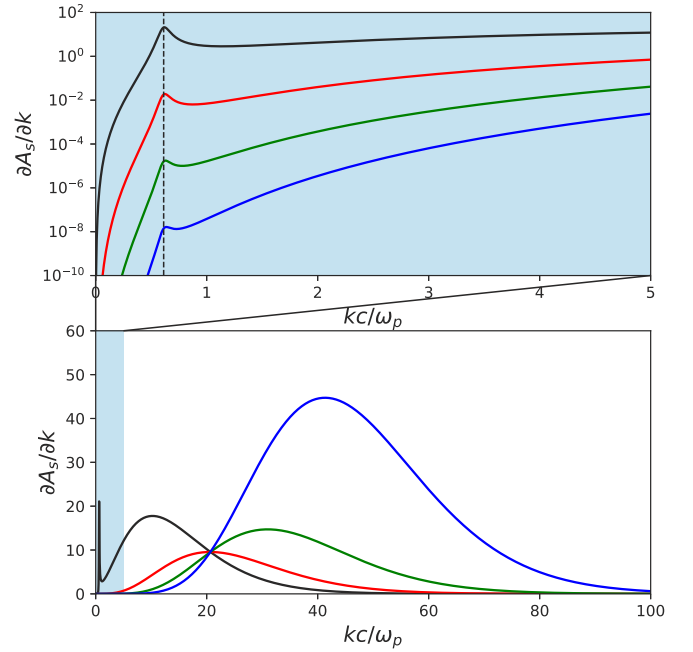


FIG. 4. The numerical results of the k distribution of $\partial A_s / \partial k$ in Eq. (55) for $s = 0, 2, 4$, and 6 , corresponding to the lines in black, red, green, and blue, respectively. The corresponding parameters are $\omega_0 = 0.5 \omega_p$, $\Gamma = 0.05 \omega_p$, $a = 0.5 z_0$, and $z_0 = 30$ nm. The dashed vertical line in the upper zoomed-in view indicates $k \simeq 0.612$, which gives the resonant energy $\omega_k = 0.5 \omega_p$.

Now, to make a comparison with the above results for the photon, we define the enhancement factor η based on Γ_0 , and organize the result in Eq. (28) as

$$\eta^o = \frac{\Gamma^o}{\Gamma_0} = A_0 \Theta_0^o + A_2 \Theta_2^o \frac{J_2}{J_0} + A_4 \Theta_4^o \frac{J_4^2}{J_0^2} \quad (53)$$

for the bright excitons and

$$\eta^e = \frac{\Gamma^e}{\Gamma_0} = A_2 \Theta_2^e \frac{J_1^2}{J_0^2} + A_4 \Theta_4^e \frac{J_1 J_3}{J_0^2} + A_6 \Theta_6^e \frac{J_3^2}{J_0^2} \quad (54)$$

for the dark excitons, where we define the result due to angular integration of the transition matrix as $\Theta_s^{o/e}$, and combine the rest of the quantity including $(ka)^s$ to the term

$$\begin{aligned} A_s &= \frac{P^2 J_0^2}{\Gamma_0} \frac{2\pi}{\hbar^2} \frac{e^2}{m^2} \int d^2\mathbf{k} (ka)^s e^{-2\beta z_0} |A(\omega_0, \mathbf{k})|^2 \\ &= \frac{3\pi c^3 a^s}{2\omega_0} \int_0^\infty dk \frac{k^{s+1} e^{-2kz_0}}{\omega_k L(k)} \frac{\Gamma / (2\pi)}{(\omega_0 - \omega_k)^2 + \Gamma^2 / 4}. \end{aligned} \quad (55)$$

The value of $\Theta_s^{o/e}$ can be easily extracted from Eqs. (40)–(43), while the value of A_s requires a further discussion.

Figure 4 displays the k distribution of A_s at $\omega_0 = 0.5 \omega_p$. Comparing with the result shown in Fig. 2, we can see that the current result is the amplitude distribution of SPP combined with the k dependence acquired from the evaluation of the decay rate. Clearly, the sharp peak appearing at a small k , which gives $\omega_k = \omega_0$, is the on-resonance peak due to the SPP with the same energy ω_0 as the exciton. Intriguingly, huge contributions can be seen in the large- k region. They can be attributed to the high-order k terms and, meanwhile,

the ‘‘Lorentzian function’’ in A_s provides a long constant tail at the off-resonance region $k \rightarrow \infty$ since ω_k approaches ω_{sp} in this region.

For the on-resonance peaking part, it can be approximated as a delta function. Therefore, for the k giving ω_k around ω_0 , the integration gives

$$A_{s1}(\omega_0) = \frac{3\pi c^3 a^s}{2\omega_0} \left(\frac{dk}{d\omega_k} \right) \Big|_{\omega_k=\omega_0} \frac{k^{s+1} e^{-2kz_0}}{\omega_0 L(k)}. \quad (56)$$

It is the spontaneous decay rate through a nondissipative SPP and can be viewed as the ‘‘radiative’’ spontaneous SPP decay. We note that for $s = 0$, the above equation gives the same result as evaluated in Ref. [24].

Conversely, for the long off-resonance tail in the large- k region, we have $L(\omega_k) \rightarrow \frac{2}{k}$, and then the maximum of the function $k^{s+2} e^{-2kz_0}$ is at $kz_0 = \frac{s+2}{2}$, which means that the SPP largely contributes to the decay around the wavelength

$$\lambda_{\text{SPP}} = \frac{2}{s+2} z_0. \quad (57)$$

Upon different system parameters, this wavelength could be very small. For example, with the parameters $\omega_p = 4$ eV and a typical value $z_0 \sim 20$ nm in a QD system, we can obtain $\lambda_{\text{SPP}} = 5$ nm corresponding to $k = 60$ for $s = 6$. We note that in the recent study by Christensen *et al.*, the authors have shown the possibility to modify the transition energy by utilizing a similar large momentum of plasmons [38]. For a real SPP material, a cutoff may need for the k integration, and the SPP dispersion may be different. However, we believe it will not make a qualitative change to the result obtained here.

Now, to focus on the off-resonance contribution by assuming $\omega_k = \omega_{sp}$ for the integration, one obtains

$$A_{s2}(\omega_0) = \frac{3\pi c^3 a^s}{2\omega_0} \frac{(s+2)!(2z_0)^{-(s+3)} \Gamma}{4\pi \omega_{sp} [(\omega_0 - \omega_{sp})^2 + \Gamma^2/4]}. \quad (58)$$

Normally, we will have $A_{s2} \gg A_{s1}$, so the behavior of the enhancement is mainly determined by A_{s2} . Figure 5 displays the numerical results of A_s with $s = 0, 2, 4$, and 6, where we have assumed $\omega_p = 4$ eV. All the exhibited scaling rules can also be observed from the expression of A_{s2} . Based on A_{s2} , for $(\omega_0 - \omega_{sp}) \gg \Gamma$, we can obtain that $A_s \propto \Gamma$ as shown in Fig. 5(a). In addition, we can expect the enhancement is peaking when $\omega \rightarrow 0$ or $\omega \rightarrow \omega_{sp}$ as shown in Fig. 5(b). Figure 5(c) displays another relation that for a fixed a/z_0 , we have $A_s \propto z_0^{-3}$ [7,31]. In the end, we see that for a fixed z_0 , $A_s \propto (a/z_0)^s$ as shown in Fig. 5(d), where A_s clearly gives a constant result for $s = 0$. Also, as we can expect, the high-order terms will have larger contributions for the systems with bigger a/z_0 .

Finally, to show the strength of the enhancement, we evaluate the η in Eqs. (53) and (54) by combining the results of A_s , J_i , and Θ_s . In the numerical study, we choose $\omega_p = 4$ eV, and the factors $J_1/J_0 = 0.8$, $J_2/J_0 = 0.7$, $J_3/J_0 = 0.6$. Their values are determined by the actual material, as discussed in Appendix C. In Fig. 6, the solid lines in red, green, blue, and purple represent the enhancement factors for HS bright ($\eta_{3/2}^o$), LS bright ($\eta_{1/2}^o$), HS dark ($\eta_{3/2}^e$), and LS dark ($\eta_{1/2}^e$) excitons, respectively. For a comparison, we show the dashed lines in red and green representing the enhancement factors with only

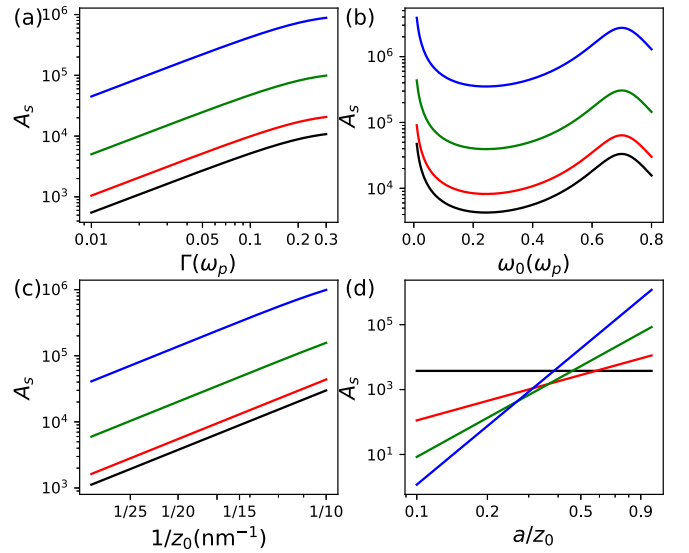


FIG. 5. The numerical results of A_s with $s = 0, 2, 4$, and 6 corresponding to the lines in black, red, green, and blue, respectively. (a) Γ dependence of A_s with $\omega_0 = 0.5 \omega_p$, $z_0 = 15$ nm, $a = 0.8 z_0$. (b) ω_0 dependence of A_s with $\Gamma = 0.2 \omega_p$, $z_0 = 15$ nm, $a = 0.8 z_0$. (c) z_0 dependence of A_s with $\omega_0 = 0.5 \omega_p$, $\Gamma = 0.2 \omega_p$, $a = 0.7 z_0$. (d) a/z_0 dependence of A_s with $\omega_0 = 0.5 \omega_p$, $\Gamma = 0.2 \omega_p$, $z_0 = 20$ nm.

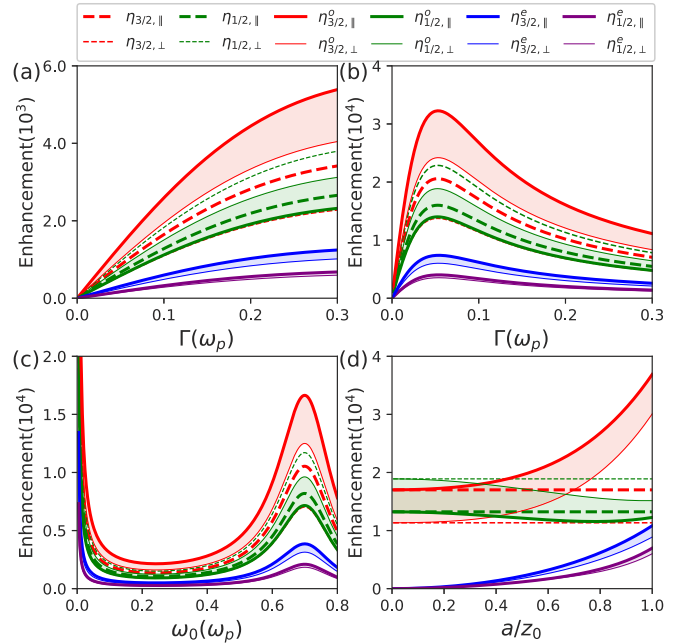


FIG. 6. The numerical results of $\eta_{3/2}^o$, $\eta_{1/2}^o$, $\eta_{3/2}^e$, and $\eta_{1/2}^e$ corresponding to the solid lines in red, green, blue, and purple, respectively. The numerical results of $\eta_{3/2}$ and $\eta_{1/2}$ corresponding to the dashed lines in red and green, respectively, indicate the dipole-only transition of the two bright excitons. The thick and thin lines represent the results for the QD with its crystal Z axis parallel (\parallel) ($\theta = \pi/2$) and perpendicular (\perp) ($\theta = 0$) to metal surface, respectively. (a) Γ dependence of η with $\omega_0 = 0.5 \omega_p$, $z_0 = 20$ nm, $a = 0.8 z_0$. (b) Γ dependence of η with $\omega_0 = 0.68 \omega_p$, $z_0 = 20$ nm, $a = 0.8 z_0$. (c) ω_0 dependence of η with $\Gamma = 0.2 \omega_p$, $z_0 = 20$ nm, $a = 0.8 z_0$. (d) a/z_0 dependence of η with $\omega_0 = 0.68 \omega_p$, $\Gamma = 0.2 \omega_p$, $z_0 = 20$ nm.

the dipole transition ($s = 0$) labeled as $\eta_{3/2}$ and $\eta_{1/2}$ for HS and LS bright excitons, respectively. In addition, the thick and thin lines represent the results for the QD with its crystal Z axis parallel ($\theta = \pi/2$) and perpendicular ($\theta = 0$) to metal surface, respectively. In general, the LS bright exciton has a larger η when the QD is perpendicular to a metal surface, while all the other states have a larger η when the QD is parallel to the surface. We note that a correlation between the orientation of the QD and the plasmon mode has been confirmed experimentally [17]. Figure 6(a) clearly shows that for $\omega_0 = 0.5 \omega_p$, the enhancement factor enlarges as Γ increases. In addition, the multipole transition for the bright states enhances the $\eta_{3/2}$ of the HS bright state, while suppresses the $\eta_{1/2}$ of the LS bright state. Figure 6(b) indicates that for $\omega_0 = 0.68 \omega_p$, η increases when $\Gamma < (\omega_0 - \omega_{sp})$, while decreases when $\Gamma > (\omega_0 - \omega_{sp})$. This can be easily seen from the Lorentz function, which shows that $\eta \propto \Gamma$ as $\Gamma \ll (\omega_0 - \omega_{sp})$, and $\eta \propto 1/\Gamma$ when $\Gamma \gg (\omega_0 - \omega_{sp})$. Significantly, the η of dark excitons gain the similar strength as the bright exciton for the system with large a/z_0 as shown in Fig. 6(d).

IV. SUMMARY

In summary, we employ a prototypical hybrid system composed of a spherical QD proximity to a metal surface to investigate the spontaneous SPP decay of the different types of QD excitons. In this system, there exist four different types of excitons distinguished by their hole states, i.e., the HS/LS hole states with odd/even parity. We find that the spontaneous SPP decay is dominant by the “nonradiative” decay into the off-resonance SPP mode, which is the hybrid mode between the SPP and dissipative bosonic pool. The transition rates of multipole state s is proportional to z_0^{-3} for a fixed a/z_0 and proportional to $(a/z_0)^s$ for a fixed z_0 . Also, the decay rate is proportional to $\frac{\Gamma}{(\omega_0 - \omega_{sp})^2 + \Gamma^2/4}$, and therefore it is $\propto \Gamma$ for $\Gamma \ll (\omega_0 - \omega_{sp})$ and $\propto 1/\Gamma$ for $\omega_0 \rightarrow \omega_{sp}$. By comparing with the spontaneous photon decay of the bright excitons, we show that the large LDOS of the SPP can strongly enhance the decay by Purcell effect, and the multipole transitions including their interference effect will further change the decay rate significantly. In particular, the dark excitons acquire a comparable decay rate with the bright exciton due to the multipole transition enhancement. The decay rate of the LS bright exciton is suppressed due to the multipole transition, while that of the HS bright exciton is enlarged. Also, the decay rate of the LS bright exciton will be enlarged as the crystal axis of the QD changes from parallel to perpendicular to the metal surface, while the decay rate of the other three excitons change in the opposite way. The above predictions of technological importance can be readily tested experimentally, and are expected to shed new light on advancing plasmonic and QD devices.

ACKNOWLEDGMENTS

We thank Dr. W. Qin for useful discussions. This work was supported by National Natural Science Foundation of China (Grants No. 11874268, No. 11634011, and No. 11974323), National Key R&D Program of China (Grant No. 2017YFA0303500), Anhui Initiative in Quantum Information Technologies (Grant No. AHY170000), and Strategic Priority

Research Program of Chinese Academy of Sciences (Grant No. XDB30000000).

APPENDIX A: DISPERSION OF THE SURFACE PLASMON POLARITONS WITH LOSSES

In this study, the dissipation of the quantization SPP is introduced by a bosonic pool, which connects with the nondissipative SPP. Here, we go through a classical way to evaluate the dissipation induced SPP frequency shifting and broadening from a lossy dielectric function. In this way, we can justify the validation of our simple approximation on the frequency shifting and broadening in the SPP quantization.

The dispersions of the SPP with a lossy dielectric function can be solved from Eq. (3) by using the Drude dielectric function

$$\epsilon_2(\omega) = 1 - \frac{\omega_p^2}{\omega(\omega + i\gamma)}, \quad (\text{A1})$$

where γ gives the dissipation rate. Since ϵ_2 is complex now, as indicated by Archambault *et al.* [30], there are two different ways to draw the dispersion lines based on Eq. (3), implying very different physics.

When one analyzes the propagation of the SPP after it is excited by a stationary monochromatic excitation localized in space, the dispersion should be given as a complex k versus a real ω as shown in Fig. 7(a). Monochromatic excitation implies that the ω should be viewed as a real value, and $\text{Im}(k)$ here describes the spatial attenuation of the SPP during its propagation.

Conversely, the dispersion with a real k should be chosen, when one analyzes the local density of states of the SPP as discussed in Ref. [30]. This is exactly the case in this study. Here, we investigate the coupling between the exciton and SPP. This coupling strength is determined by the SPP density of states at a certain wave vector k , which provides the spatial distribution of the SPP field and thus should be considered as a good quantum number. Then, when the dissipation is introduced due to a lossy dielectric function or bosonic pool, the SPP field will keep a real wave vector k and gain a complex frequency ω , with the real part indicating the shifted dispersion and the imaginary part indicating the finite lifetime and broadening in the frequency. As shown in Fig. 7(b), when the dispersion is given by a real k versus a complex ω , we find that the difference between the $\text{Re}(\omega)$ and lossless $\omega_0(k)$ (for $\gamma = 0$), defined as $\Delta[\text{Re}(\omega)]$, is very small, and the $\text{Im}(\omega) \rightarrow \gamma/2$ for $k \rightarrow \infty$. This result justifies our approximation, i.e., $\delta\omega = 0$ and $\Gamma = \text{constant}$ for the effect of the bosonic pool.

APPENDIX B: GREEN'S FUNCTION AND DENSITY OF STATES FOR THE DRESSED SPP

Here, we restrict our discussion within the Green's function of a bosonic operator. For the sake of completeness, we start from a nondissipative bosonic field. Now, assume there is a well-defined bosonic field with its Hamiltonian written as

$$H = \sum_k \hbar \omega_k \hat{a}_k^\dagger \hat{a}_k \quad (\text{B1})$$

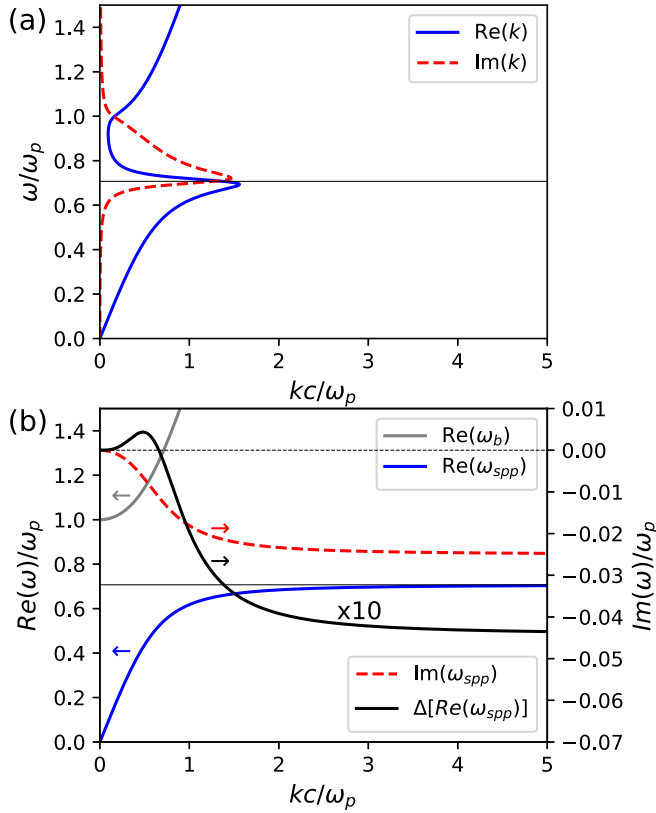


FIG. 7. The dispersion of the SPP with a lossy dielectric function at $\gamma = 0.05 \omega_p$. (a) The dispersion with a real frequency ω . The blue solid (red dashed) line indicates the real (imaginary) part of k . (b) The dispersion with a real wave vector k . The blue solid (red dashed) line indicates the real (imaginary) part of ω . The black solid line indicates the difference between the dispersion line with and without the loss.

with an assumption that $\omega_k = \omega_{-k}$. The corresponding Green's function is defined as

$$G(\mathbf{k}, t - t') = -i \langle 0 | T A_{\mathbf{k}}(t) A_{-\mathbf{k}}(t') | 0 \rangle, \quad (\text{B2})$$

where the operator T is the time order operator and $|0\rangle$ is the particle vacuum state. For the bosonic field described by (B1), the operator $A_{\mathbf{k}}(t)$ reads as

$$A_{\mathbf{k}}(t) = a_{\mathbf{k}} e^{-i\omega_{\mathbf{k}} t} + a_{-\mathbf{k}}^{\dagger} e^{i\omega_{\mathbf{k}} t}. \quad (\text{B3})$$

By using the relations that

$$\langle 0 | a_{\mathbf{k}} a_{\mathbf{k}}^{\dagger} | 0 \rangle = 1 \quad \text{and} \quad \langle 0 | a_{\mathbf{k}}^{\dagger} a_{\mathbf{k}} | 0 \rangle = 0, \quad (\text{B4})$$

we obtain

$$G(\mathbf{k}, t - t') = -i [\Theta(t - t') e^{-i\omega_{\mathbf{k}}(t-t')} + \Theta(t' - t) e^{i\omega_{\mathbf{k}}(t-t')}]. \quad (\text{B5})$$

Then, the Fourier transform of the Green's function gives

$$G(\mathbf{k}, \omega) = \frac{1}{\omega - \omega_{\mathbf{k}} + i\eta} - \frac{1}{\omega + \omega_{\mathbf{k}} - i\eta}, \quad (\text{B6})$$

where η is an infinitesimal constant. This is the Green's function of the free bosonic field described by Eq. (B1). In the main text, for simplicity, we have ignored the term with $(\omega + \omega_{\mathbf{k}})$ because it has much smaller contribution than that of the $(\omega - \omega_{\mathbf{k}})$ term at $\omega \rightarrow \omega_{\mathbf{k}}$.

Now we turn to the dressed SPP (dSPP) described by the Hamiltonian

$$H = \sum_{\mathbf{k}} \int_0^{\infty} d\omega \hbar \omega \hat{f}_{\mathbf{k},\omega}^{\dagger} \hat{f}_{\mathbf{k},\omega}. \quad (\text{B7})$$

For this Hamiltonian, we write

$$A_{\mathbf{k}}(t) = \int_0^{\infty} d\omega [N(\omega, \mathbf{k}) \hat{f}_{\mathbf{k},\omega} e^{-i\omega t} + N^*(\omega, -\mathbf{k}) \hat{f}_{-\mathbf{k},\omega}^{\dagger} e^{i\omega t}], \quad (\text{B8})$$

where $N(\omega, \mathbf{k})$ is a normalization factor satisfying

$$\int_0^{\infty} d\omega |N(\omega, \mathbf{k})|^2 = 1. \quad (\text{B9})$$

Now by inserting the new $A_{\mathbf{k}}(t)$ in Eq. (B2) and applying the new commutation relations

$$\begin{aligned} \langle 0 | f_{\mathbf{k},\omega} f_{\mathbf{k},\omega}^{\dagger} | 0 \rangle &= \delta(\omega - \omega'), \\ \langle 0 | f_{\mathbf{k},\omega}^{\dagger} f_{\mathbf{k},\omega} | 0 \rangle &= 0, \end{aligned} \quad (\text{B10})$$

we can easily obtain the relation between the Green's function and normalization factor as

$$G(\omega, \mathbf{k}) = \int_0^{\infty} d\omega' \left[\frac{|N(\omega', \mathbf{k})|^2}{\omega - \omega' + i\eta} - \frac{|N(\omega', -\mathbf{k})|^2}{\omega + \omega' - i\eta} \right] d\omega'. \quad (\text{B11})$$

Apparently, when we chose the normalization factor $|N(\omega, \mathbf{k})|^2$ to be $\delta(\omega - \omega_{\mathbf{k}})$, the above equation can be reduced to the nondissipative form in Eq. (B6). Here, the actual form $N(\omega, \mathbf{k})$ cannot be determined and thus it is not realistic to obtain an analytic result for $G(\omega, \mathbf{k})$. However, by focusing on the imaginary part of the above equation, a generic relation can be obtained as

$$\begin{aligned} \text{Im}[G(\omega, \mathbf{k})] &= -\pi \int_0^{\infty} d\omega' [|N(\omega', \mathbf{k})|^2 \delta(\omega - \omega') \\ &\quad + |N(\omega', -\mathbf{k})|^2 \delta(\omega + \omega')] d\omega'. \end{aligned} \quad (\text{B12})$$

For the system we consider, we keep only the term with $\omega > 0$, so that

$$\text{Im}[G(\omega, \mathbf{k})] = -\pi |N(\omega, \mathbf{k})|^2, \quad (\text{B13})$$

which has been used in the main text. The physical meaning of the normalization factor can be interpreted as the density of states of the dSPP. Consequently, we obtain the relation between the Green's function and density of states of the dSPP.

APPENDIX C: RADIAL FUNCTION R_l FOR STATES WITH $F = \frac{3}{2}$

The Hamiltonian of the hole states in the QD with a zinc-blende structure can be written as [35]

$$H_h = \frac{\gamma_1}{2m_0} \left[p^2 - \frac{\mu}{9} (\mathbf{P}^{(2)} \cdot \mathbf{J}^{(2)}) \right] + V_{\text{QD}}(r), \quad (\text{C1})$$

where $\mathbf{P}^{(2)}$ and $\mathbf{J}^{(2)}$ are second-rank spherical tensors for linear and angular momenta, and $\mu = \frac{2\gamma_2}{\gamma_1}$ is determined by Luttinger parameters γ_1 and γ_2 . This equation was deduced from Luttinger Hamiltonian [34], by considering the so-called "spherical approximation" with $\gamma_2 = \gamma_3$. The above equation

is valid in the limit of strong spin-orbit coupling between valence bands, and the spherical approximation is valid for most of crystals with the diamond and zinc-blende structures [35]. For simplicity, the confined potential $V_{\text{QD}}(r)$ is considered to be a spherical infinity potential well with the form

$$V(r) = \begin{cases} 0, & r < a \\ +\infty, & r \geq a \end{cases} \quad (\text{C2})$$

where a is the radius of the QD. The existing SOC term in the Hamiltonian mixing the typical heavy- and light-hole bands in the bulk system, and the corresponding wave function has been shown to satisfy the following function [32,39]:

$$\begin{pmatrix} -(1+C_1)H_{11} & C_2H_{12} \\ C_2H_{21} & -(1-C_1)H_{22} \end{pmatrix} \begin{pmatrix} R_l \\ R_{l+2} \end{pmatrix} = \frac{2m_0E}{\gamma_1\hbar^2} \begin{pmatrix} R_l \\ R_{l+2} \end{pmatrix}, \quad (\text{C3})$$

where E denotes the eigenenergy,

$$H_{11} = \frac{d^2}{dr^2} + \frac{2}{r} \frac{d}{dr} - \frac{l(l+1)}{r^2}, \quad (\text{C4})$$

$$H_{12} = \frac{d^2}{dr^2} + \frac{2l+5}{r} \frac{d}{dr} + \frac{(l+1)(l+3)}{r^2}, \quad (\text{C5})$$

$$H_{21} = \frac{d^2}{dr^2} - \frac{2l+1}{r} \frac{d}{dr} + \frac{l(l+2)}{r^2}, \quad (\text{C6})$$

$$H_{22} = \frac{d^2}{dr^2} + \frac{2}{r} \frac{d}{dr} - \frac{(l+2)(l+3)}{r^2}, \quad (\text{C7})$$

and the radial part of the wave function R_l is mixed by heavy- and light-hole solutions as

$$R_l(r) = \frac{A}{a^{3/2}} b_l \left[j_l(k_H r) - \frac{j_l(k_H a)}{j_l(k_L a)} j_l(k_L r) \right], \quad (\text{C8})$$

where j_l is the spherical Bessel function of l th order; $k_H = \sqrt{2m_{hh}E_h}/\hbar$ and $k_L = \sqrt{2m_{lh}E_l}/\hbar$ with effective masses of heavy hole $m_{hh} = m_0/(\gamma_1 - 2\gamma_2)$ and light hole $m_{lh} = m_0/(\gamma_1 + 2\gamma_2)$. The above form of the wave function guarantees the boundary condition

$$R_l(a) = 0 \quad (\text{C9})$$

by noticing the relations [39]

$$H_{12}j_{l+2} = k^2 j_l, \quad (\text{C10})$$

$$H_{21}j_l = k^2 j_{l+2}, \quad (\text{C11})$$

the analytic form of the solutions can be easily obtained. For the even parity state with $l = 0, 2$, $C_1 = 0$, and $C_2 = \mu$,

$$R_0 = \frac{A}{a^{3/2}} [j_0(k_H r) - \eta_0 j_0(k_L r)], \quad (\text{C12})$$

$$R_2 = \frac{A}{a^{3/2}} [j_2(k_H r) - \eta_2 j_2(k_L r)], \quad (\text{C13})$$

and the energy of the state is determined from

$$\eta_0 + \eta_2 = 0, \quad (\text{C14})$$

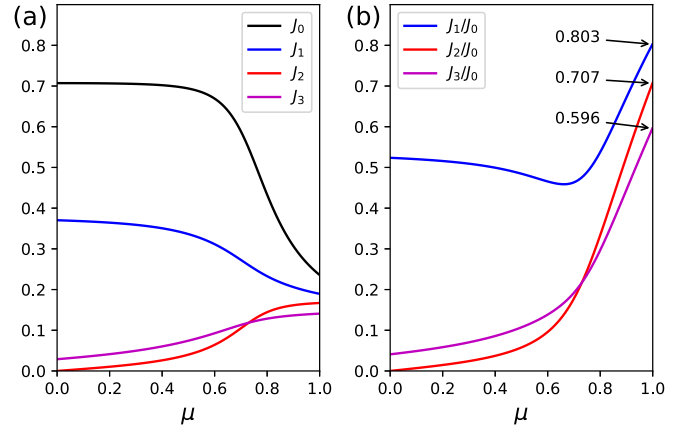


FIG. 8. The values of J_i and J_i/J_0 as a function of μ .

where $\eta_l = j_l(k_H a)/j_l(k_L a)$. The same result has been shown in Ref. [32]. For the odd parity state with $l = 1, 3$, $C_1 = -\frac{4}{3}\mu$, and $C_2 = \frac{3}{5}\mu$, we find

$$R_1 = \frac{A}{a^{3/2}} [j_1(k_H r) - \eta_1 j_1(k_L r)], \quad (\text{C15})$$

$$R_3 = \frac{3A}{a^{3/2}} [j_3(k_H r) - \eta_3 j_3(k_L r)], \quad (\text{C16})$$

and the energy of the state is determined from

$$\eta_1 + 9\eta_3 = 0. \quad (\text{C17})$$

Finally, the normalization factor A can be obtained by the normalizing condition

$$\int dr r^2 [R_l^2 + R_{l+2}^2] = 1. \quad (\text{C18})$$

The result of R_l relies on the ratio of the effective mass $\beta = m_{lh}/m_{hh}$, and thus the SOC strength μ as

$$\beta = \frac{1-\mu}{1+\mu}. \quad (\text{C19})$$

In Fig. 8, we show the numerical result of J_l in Eq. (38) at different μ values. It eventually gives upper boundaries for $J_1/J_0 = 0.803$, $J_2/J_0 = 0.707$, $J_3/J_0 = 0.596$ at the large SOC limit.

APPENDIX D: MATRIX ELEMENT $\langle S\alpha | \mathbf{e}_p \cdot \hat{\mathbf{p}} | u_\mu \rangle$

By using the Bloch function u_μ of valence band Γ_{8v} in Eq. (27), we can evaluate transition between state $|J, \mu\rangle = |\frac{3}{2}, \frac{3}{2}\rangle$ and $|S \uparrow\rangle$ as

$$\begin{aligned} \langle S_{\frac{3}{2}, \uparrow} | &= \langle S \uparrow | \mathbf{e}_p \cdot \hat{\mathbf{p}} | u_{3/2} \rangle \\ &= \mathbf{e}_p \cdot \langle S \uparrow | \hat{\mathbf{p}}_- \left| \frac{1}{\sqrt{2}} (X + iY) \uparrow \right\rangle \\ &= \frac{1}{\sqrt{2}} P \mathbf{e}_p \cdot (\hat{X} + i\hat{Y}), \end{aligned} \quad (\text{D1})$$

where $P = \langle S | \hat{p}_X | X \rangle = \langle S | \hat{p}_Y | Y \rangle = \langle S | \hat{p}_Z | Z \rangle$ is the Kane interband transition matrix element for the cubic lattice with

isotropic values. Similarly, we can obtain the relations

$$\begin{aligned} C_{\frac{3}{2},\uparrow} &= \frac{1}{\sqrt{2}} P \mathbf{e}_p \cdot (\hat{X} + i\hat{Y}), \\ C_{\frac{3}{2},\downarrow} &= 0, \\ C_{-\frac{3}{2},\downarrow} &= \frac{i}{\sqrt{2}} P \mathbf{e}_p \cdot (\hat{X} - i\hat{Y}), \\ C_{-\frac{3}{2},\uparrow} &= 0 \end{aligned} \quad (\text{D2})$$

for the transitions to heavy hole, and

$$\begin{aligned} C_{\frac{1}{2},\uparrow} &= -\sqrt{\frac{2}{3}} P \mathbf{e}_p \cdot \hat{Z}, \\ C_{\frac{1}{2},\downarrow} &= \frac{1}{\sqrt{6}} P \mathbf{e}_p \cdot (\hat{X} + i\hat{Y}), \\ C_{-\frac{1}{2},\downarrow} &= i\sqrt{\frac{2}{3}} P \mathbf{e}_p \cdot \hat{Z}, \\ C_{-\frac{1}{2},\uparrow} &= -\frac{i}{\sqrt{6}} P \mathbf{e}_p \cdot (\hat{X} - i\hat{Y}) \end{aligned} \quad (\text{D3})$$

for the transitions to light hole. To evaluate the dot products in above relations, we first write the polarization of SPP in a more general form

$$\mathbf{e}_p^{xyz} = \cos \phi \hat{x} + \sin \phi \hat{y} + i \frac{k}{\beta} \hat{z}, \quad (\text{D4})$$

which indicates the polarization of the SPP propagating in different azimuthal angle ϕ of the coordinate xyz . The transition from the coordinate xyz to the coordinate XYZ of the QD crystal lattice can be simply considered as a rotation by angle θ about the y axis because the self-rotation angle of QD about the Z axis will not affect the result and the rotation about the z axis will be integrated. So, the polarization of the SPP in XYZ is written as

$$\mathbf{e}_p^{XYZ} = \begin{bmatrix} \cos \theta & 0 & -\sin \theta \\ 0 & 1 & 0 \\ \sin \theta & 0 & \cos \theta \end{bmatrix} \mathbf{e}_p^{xyz} \quad (\text{D5})$$

and we obtain

$$\mathbf{e}_p \cdot (\hat{X} \pm i\hat{Y}) = \cos \theta \cos \phi - i \frac{k}{\beta} \sin \theta \pm i \sin \phi \quad (\text{D6})$$

and

$$\mathbf{e}_p \cdot \hat{Z} = \sin \theta \cos \phi + i \frac{k}{\beta} \cos \theta. \quad (\text{D7})$$

In addition, by doing the integration for azimuthal angle ϕ of xyz , we obtain that

$$\int \frac{d\phi}{2\pi} |\mathbf{e}_p \cdot (\hat{X} \pm i\hat{Y})|^2 = \frac{1 + \cos^2 \theta}{2} + \frac{k^2}{\beta^2} \sin^2 \theta \quad (\text{D8})$$

and

$$\int \frac{d\phi}{2\pi} |\mathbf{e}_p \cdot \hat{Z}|^2 = \frac{\sin^2 \theta}{2} + \frac{k^2}{\beta^2} \cos^2 \theta \quad (\text{D9})$$

and then

$$\langle |C_{\frac{3}{2},\uparrow}|^2 \rangle = \langle |C_{-\frac{3}{2},\downarrow}|^2 \rangle = P^2 \left(\frac{3}{4} - \frac{1}{4} \cos^2 \theta \right), \quad (\text{D10})$$

$$\langle |C_{\frac{3}{2},\downarrow}|^2 \rangle = \langle |C_{-\frac{3}{2},\uparrow}|^2 \rangle = 0, \quad (\text{D11})$$

$$\langle |C_{\frac{1}{2},\uparrow}|^2 \rangle = \langle |C_{-\frac{1}{2},\downarrow}|^2 \rangle = P^2 \left(\frac{1}{3} + \frac{1}{3} \cos^2 \theta \right), \quad (\text{D12})$$

$$\langle |C_{\frac{1}{2},\downarrow}|^2 \rangle = \langle |C_{-\frac{1}{2},\uparrow}|^2 \rangle = P^2 \left(\frac{1}{4} - \frac{1}{12} \cos^2 \theta \right). \quad (\text{D13})$$

APPENDIX E: INTEGRAND PART OF THE EMISSION RATE

In this Appendix, we give some details about the evaluation of the integrand part $T_{M,\alpha}(\mathbf{k})$ of the decay rate as in Eq. (36). By explicitly inserting the results of the angular integration (37) of the transition matrix, for odd state, we obtain that

$$T_{\pm\frac{1}{2},\alpha}^o = \left| J_0 C_{\pm\frac{1}{2},\alpha} - \frac{(ka)^2}{10} J_2 \left(C_{\pm\frac{1}{2},\alpha} \mp \frac{i2\sqrt{3}}{3} C_{\pm\frac{3}{2},\alpha} + \frac{\sqrt{3}}{3} C_{\mp\frac{3}{2},\alpha} \right) \right|^2 \quad (\text{E1})$$

and

$$T_{\pm\frac{3}{2},\alpha}^o = \left| J_0 C_{\pm\frac{3}{2},\alpha} + \frac{(ka)^2}{10} J_2 \left(C_{\pm\frac{3}{2},\alpha} \pm \frac{i2\sqrt{3}}{3} C_{\pm\frac{1}{2},\alpha} - \frac{\sqrt{3}}{3} C_{\mp\frac{1}{2},\alpha} \right) \right|^2. \quad (\text{E2})$$

Then, by inserting the value of $C_{\mu\alpha}$, we obtain that

$$\overline{T_{\frac{1}{2},\uparrow}^o} = P^2 \left(J_0^2 - J_0 J_2 \frac{(ka)^2}{5} \right) \left(\frac{1}{4} - \frac{1}{12} \cos^2 \theta \right) + P^2 J_2^2 \frac{(ka)^4}{10^2} \left(\frac{5}{4} - \frac{5}{12} \cos^2 \theta \right), \quad (\text{E3})$$

$$\overline{T_{\frac{1}{2},\downarrow}^o} = P^2 \left(J_0^2 - J_0 J_2 \frac{(ka)^2}{5} \right) \left(\frac{1}{3} + \frac{1}{3} \cos^2 \theta \right) + P^2 J_2^2 \frac{(ka)^4}{10^2} \left(\frac{7}{12} + \frac{1}{4} \cos^2 \theta \right), \quad (\text{E4})$$

$$\overline{T_{\frac{3}{2},\uparrow}^o} = P^2 \left(J_0^2 + J_0 J_2 \frac{(ka)^2}{5} \right) \left(\frac{3}{4} - \frac{1}{4} \cos^2 \theta \right) + P^2 J_2^2 \frac{(ka)^4}{10^2} \left(\frac{23}{18} + \frac{1}{6} \cos^2 \theta \right), \quad (\text{E5})$$

and

$$\overline{T_{\frac{3}{2},\downarrow}^o} = P^2 J_2^2 \frac{(ka)^4}{10^2} \frac{4}{9}. \quad (\text{E6})$$

Following the same procedure as in the case of the odd state, the results of the even states are

$$\overline{T_{\frac{1}{2},\uparrow}^e} = P^2 J_1^2 \frac{(ka)^2}{45} \left(\frac{43}{12} - \frac{3}{4} \cos^2 \theta \right) - P^2 J_1 J_3 \frac{(ka)^4}{105} \left(\frac{1}{12} + \frac{5}{12} \cos^2 \theta \right) + P^2 J_3^2 \frac{(ka)^6}{5 \times 14^2} \left(\frac{5}{6} + \frac{1}{6} \cos^2 \theta \right), \quad (E7)$$

$$\overline{T_{\frac{1}{2},\downarrow}^e} = P^2 J_1^2 \frac{(ka)^2}{45} \left(\frac{19}{12} + \frac{5}{4} \cos^2 \theta \right) - P^2 J_1 J_3 \frac{(ka)^4}{105} \left(\frac{11}{12} + \frac{7}{12} \cos^2 \theta \right) + P^2 J_3^2 \frac{(ka)^6}{5 \times 14^2} \left(\frac{5}{6} + \frac{1}{6} \cos^2 \theta \right), \quad (E8)$$

$$\overline{T_{\frac{3}{2},\uparrow}^e} = P^2 J_1^2 \frac{(ka)^2}{5} \left(\frac{31}{36} - \frac{5}{36} \cos^2 \theta \right) + P^2 J_1 J_3 \frac{(ka)^4}{105} \left(\frac{3}{4} - \frac{1}{4} \cos^2 \theta \right) + P^2 J_3^2 \frac{(ka)^6}{5 \times 42^2} \left(\frac{3}{2} - \frac{1}{2} \cos^2 \theta \right), \quad (E9)$$

and

$$\overline{T_{\frac{3}{2},\downarrow}^e} = P^2 J_1^2 \frac{(ka)^2}{5} \left(\frac{1}{12} - \frac{1}{36} \cos^2 \theta \right) + P^2 J_3^2 \frac{(ka)^6}{5 \times 42^2} \left(\frac{7}{4} + \frac{3}{4} \cos^2 \theta \right). \quad (E10)$$

-
- [1] W. L. Barnes, A. Dereux, and T. W. Ebbesen, Surface plasmon subwavelength optics, *Nature (London)* **424**, 824 (2003).
- [2] N. Fang, Sub-diffraction-limited optical imaging with a silver superlens, *Science* **308**, 534 (2005).
- [3] H. Wei, Z. Wang, X. Tian, M. Käll, and H. Xu, Cascaded logic gates in nanophotonic plasmon networks, *Nat. Commun.* **2**, 387 (2011).
- [4] K. Kneipp, Y. Wang, H. Kneipp, L. T. Perelman, I. Itzkan, R. R. Dasari, and M. S. Feld, Single Molecule Detection Using Surface-Enhanced Raman Scattering (SERS), *Phys. Rev. Lett.* **78**, 1667 (1997).
- [5] H. Xu, E. J. Bjerneld, M. Käll, and L. Börjesson, Spectroscopy of Single Hemoglobin Molecules by Surface Enhanced Raman Scattering, *Phys. Rev. Lett.* **83**, 4357 (1999).
- [6] A. V. Zayats and I. I. Smolyaninov, Near-field photonics: Surface plasmon polaritons and localized surface plasmons, *J. Opt. A: Pure Appl. Opt.* **5**, S16 (2003).
- [7] N. Rivera, I. Kaminer, B. Zhen, J. D. Joannopoulos, and M. Soljačić, Shrinking light to allow forbidden transitions on the atomic scale, *Science* **353**, 263 (2016).
- [8] A. M. Kern and O. J. F. Martin, Strong enhancement of forbidden atomic transitions using plasmonic nanostructures, *Phys. Rev. A* **85**, 022501 (2012).
- [9] L. Martín-Moreno, F. J. G. de Abajo, and F. J. García-Vidal, Ultraefficient Coupling of a Quantum Emitter to the Tunable Guided Plasmons of a Carbon Nanotube, *Phys. Rev. Lett.* **115**, 173601 (2015).
- [10] T. Neuman, R. Esteban, D. Casanova, F. J. García-Vidal, and J. Aizpurua, Coupling of molecular emitters and plasmonic cavities beyond the point-dipole approximation, *Nano Lett.* **18**, 2358 (2018).
- [11] Y. Zhang, Z.-C. Dong, and J. Aizpurua, Influence of the chemical structure on molecular light emission in strongly localized plasmonic fields, *J. Phys. Chem. C* **124**, 4674 (2020).
- [12] P. Lodahl, S. Mahmoodian, and S. Stobbe, Interfacing single photons and single quantum dots with photonic nanostructures, *Rev. Mod. Phys.* **87**, 347 (2015).
- [13] Y. Shirasaki, G. J. Supran, M. G. Bawendi, and V. Bulović, Emergence of colloidal quantum-dot light-emitting technologies, *Nat. Photonics* **7**, 13 (2013).
- [14] H. Shen, Q. Gao, Y. Zhang, Y. Lin, Q. Lin, Z. Li, L. Chen, Z. Zeng, X. Li, Y. Jia, S. Wang, Z. Du, L. S. Li, and Z. Zhang, Visible quantum dot light-emitting diodes with simultaneous high brightness and efficiency, *Nat. Photonics* **13**, 192 (2019).
- [15] C.-H. M. Chuang, P. R. Brown, V. Bulović, and M. G. Bawendi, Improved performance and stability in quantum dot solar cells through band alignment engineering, *Nat. Mater.* **13**, 796 (2014).
- [16] H. J. Kimble, The quantum internet, *Nature (London)* **453**, 1023 (2008).
- [17] M. L. Andersen, S. Stobbe, A. S. Sørensen, and P. Lodahl, Strongly modified plasmon-matter interaction with mesoscopic quantum emitters, *Nat. Phys.* **7**, 215 (2011).
- [18] J. Johansen, S. Stobbe, I. S. Nikolaev, T. Lund-Hansen, P. T. Kristensen, J. M. Hvam, W. L. Vos, and P. Lodahl, Size dependence of the wavefunction of self-assembled InAs quantum dots from time-resolved optical measurements, *Phys. Rev. B* **77**, 073303 (2008).
- [19] S. Stobbe, J. M. Hvam, and P. Lodahl, On the interpretation of wave function overlaps in quantum dots, *Phys. Status Solidi B* **248**, 855 (2011).
- [20] C. Qian, X. Xie, J. Yang, K. Peng, S. Wu, F. Song, S. Sun, J. Dang, Y. Yu, M. J. Steer, I. G. Thayne, K. Jin, C. Gu, and X. Xu, Enhanced Strong Interaction between Nanocavities and p-shell Excitons Beyond the Dipole Approximation, *Phys. Rev. Lett.* **122**, 087401 (2019).
- [21] P. Tighineanu, M. L. Andersen, A. S. Sørensen, S. Stobbe, and P. Lodahl, Probing Electric and Magnetic Vacuum Fluctuations with Quantum Dots, *Phys. Rev. Lett.* **113**, 043601 (2014).
- [22] M. Cotrufo and A. Fiore, Spontaneous emission from dipole-forbidden transitions in semiconductor quantum dots, *Phys. Rev. B* **92**, 125302 (2015).
- [23] E. Rusak, J. Straubel, P. Gładysz, M. Göddel, A. Kedziorski, M. Kühn, F. Weigend, C. Rockstuhl, and K. Słowik, Enhancement of and interference among higher order multipole transitions in molecules near a plasmonic nanoantenna, *Nat. Commun.* **10**, 5775 (2019).
- [24] A. Archambault, F. Marquier, J.-J. Greffet, and C. Arnold, Quantum theory of spontaneous and stimulated emission of surface plasmons, *Phys. Rev. B* **82**, 035411 (2010).

- [25] S. Scheel and S. Buhmann, Macroscopic quantum electrodynamics - Concepts and applications, *Acta Phys. Slovaca* **58**, 675 (2008).
- [26] A. Manjavacas, F. J. García de Abajo, and P. Nordlander, Quantum plexcitonics: Strongly interacting plasmons and excitons, *Nano Lett.* **11**, 2318 (2011).
- [27] M. S. Tame, C. Lee, J. Lee, D. Ballester, M. Paternostro, A. V. Zayats, and M. S. Kim, Single-Photon Excitation of Surface Plasmon Polaritons, *Phys. Rev. Lett.* **101**, 190504 (2008).
- [28] M. S. Tame, K. R. McEnery, Ş. K. Özdemir, J. Lee, S. A. Maier, and M. S. Kim, Quantum plasmonics, *Nat. Phys.* **9**, 329 (2013).
- [29] B. Huttner and S. M. Barnett, Quantization of the electromagnetic field in dielectrics, *Phys. Rev. A* **46**, 4306 (1992).
- [30] A. Archambault, T. V. Teperik, F. Marquier, and J. J. Greffet, Surface plasmon Fourier optics, *Phys. Rev. B* **79**, 195414 (2009).
- [31] P. A. D. Gonçalves, T. Christensen, N. Rivera, A.-P. Jauho, N. A. Mortensen, and M. Soljačić, Plasmon–emitter interactions at the nanoscale, *Nat. Commun.* **11**, 366 (2020).
- [32] A. L. Efros, Luminescence polarization of CdSe microcrystals, *Phys. Rev. B* **46**, 7448 (1992).
- [33] A. L. Efros, M. Rosen, M. Kuno, M. Nirmal, D. J. Norris, and M. Bawendi, Band-edge exciton in quantum dots of semiconductors with a degenerate valence band: Dark and bright exciton states, *Phys. Rev. B* **54**, 4843 (1996).
- [34] J. M. Luttinger, Quantum theory of cyclotron resonance in semiconductors: General theory, *Phys. Rev.* **102**, 1030 (1956).
- [35] A. Baldereschi and N. O. Lipari, Spherical model of shallow acceptor states in semiconductors, *Phys. Rev. B* **8**, 2697 (1973).
- [36] N. O. Lipari and A. Baldereschi, Angular Momentum Theory and Localized States in Solids. Investigation of Shallow Acceptor States in Semiconductors, *Phys. Rev. Lett.* **25**, 1660 (1970).
- [37] A. González-Tudela, P. A. Huidobro, L. Martín-Moreno, C. Tejedor, and F. J. García-Vidal, Theory of Strong Coupling between Quantum Emitters and Propagating Surface Plasmons, *Phys. Rev. Lett.* **110**, 126801 (2013).
- [38] T. Christensen, I. Kaminer, M. Orenstein, N. Rivera, Y. Kurman, M. Soljačić, S. Tsesses, and J. D. Joannopoulos, Control of semiconductor emitter frequency by increasing polariton momenta, *Nat. Photonics* **12**, 423 (2018).
- [39] J.-b. Xia, Electronic structure of quantum spheres and quantum wires, *J. Lumin.* **70**, 120 (1996).